Article:

Peltzer, G., Brown, N.D., Mériaux, A.-S.B. et al. (5 more authors) (2020) Stable rate of slip along the Karakax section of the Altyn Tagh Fault from observation of inter-glacial and post-glacial offset morphology and surface dating. Journal of Geophysical Research: Solid Earth, 125 (5). e2019JB018893. ISSN 2169-9313

https://doi.org/10.1029/2019jb018893

Stable rate of slip along the Karakax section of the Altyn Tagh Fault from observation of inter-glacial and post-glacial offset morphology and surface dating

Gilles Peltzer [1,2], Nathan D. Brown[1*], Anne-Sophie B. Meriaux [4], Jerome van der Woerd [3], Edward J. Rhodes [5], Robert C. Finkel [6], Frederick J. Ryerson [6], James Hollingsworth [7]

[1]University of California Los Angeles, 595 Charles Young Drive East, Los Angeles, CA95095, USA
[2]Jet Propulsion Laboratory, California Institute of Technology, CA, USA
[3]University of Strasbourg, Strasbourg, France
[4]Newcastle University, Newcastle Upon Tyne, United Kingdom
[5]University of Sheffield, Department of Geography, Sheffield, United Kingdom
[6]LLNL, Livermore, CA, USA
[7]ISTerre Institute of Earth Sciences, Saint Martin d'Hères, France

Key Points:

- Offset alluvial fans in Karakax Valley record sinistral displacement history along Altyn Tagh Fault
- Terrace ages determined by OSL and CRN dating methods yield fault slip-rate of 2.6 mm/a over 115 ka
- Seismic clustering or variable erosion rate linked to climate may explain observed fault scarp degradation variations

*Current address, Department of Earth and Planetary Science, University of California, Berkeley, CA, USA and Berkeley Geochronology Center, 2455 Ridge Road, Berkeley, CA, USA

Corresponding author: Gilles Peltzer, peltzer@epss.ucla.edu

Abstract

Digital elevation maps obtained using TanDEM-X and Pleiades data combined with newly obtained surface age estimates using Cosmogenic Radionuclide (CRN) and Optically Simulated Luminescence (OSL) methods are used to quantify the slip-rate along the western section of the Altyn Tagh fault in southern Xinjiang. The reconstruction of the conical shape of massive alluvial fans inferred to be from the Eemian (115±7 ka) from CRN dating shows consistent left-lateral offsets of 300±20 m, yielding a slip rate of 2.6±0.3 mm/yr. Successive episodes of incision have left cut terraces inset in wide canyons, 10-25 m below the fans' surface. The incision was followed by the deposition of a broad terrace of early Holocene age, which is re-incised by modern stream channels. Near the village of Shanxili, a 200 m-wide valley is partially dammed by a shutter ridge displaced by the fault. A fill terrace deposited upstream from the ridge has an OSL age of 8.8±0.6 ka. The 23±2 m offset of the riser incising the terrace indicates a minimum post-depositional movement on the fault, yielding a Holocene rate of 2.6±0.5 mm/yr, consistent with the 115 ka-average slip rate. Scarp degradation analysis using mass diffusion reveals a non-linear relationship between fault displacement and degradation coefficient along the progressively exposed fault scarp, a pattern suggesting either seismic clustering or variable diffusion rate since the Eemian. Together with the Gozha Co-Longmu Co fault to the south, the Karakax section of the Altyn Tagh Fault contributes to the eastward movement of the western corner of Tibet.

1 Introduction

The westernmost section of the Altyn Tagh Fault runs along the upper Karakax Valley in the Western Kunlun range (Figure 1). The high elevation of the valley results in abundant quaternary deposits associated with the advances and retreats of neighboring glaciers, especially on the north side of the valley where massive alluvial fans form the piedmont of the Kunlun mountains down to the Karakax River. The sinistral, strike-slip nature of the fault has long been recognized from its morphology on Landsat images (Molnar & Tapponnier, 1975; Tapponnier & Molnar, 1977; Armijo et al., 1989, e.g.,) and lateral displacements of glacial and post-glacial features have also been mapped from space using the early generation SPOT images (Peltzer et al., 1989). Despite the abundance of geomorphic markers displaced by recent movement on this fault section, the estimation of the long-term slip rate on the fault is still debated due to the difficulty to assign a definite age to displaced geomorphic features. Early estimations of the slip rate based on surface dating using cosmogenic methods indicate values of 12-23 mm/yr (Ryerson et al., 1999) and 14-18 mm/yr (Li et al., 2008), while Gong et al. (2017) proposed a slower slip-rate of 6-7 mm/yr using OSL dating of a set of terraces and independent estimates of lateral offsets of associated risers. Large error bars on age determinations and ambiguous associations of surface ages with displaced risers may explain the discrepancy between these studies. Meanwhile, a sub-centimeter slip-rate of 6-7 mm/yr have been estimated for the late Holocene period using 14C dating and the characterization of up to four repeated slip-events of 6-7 m each, every ∼900 years, recorded in lateral offsets of small incising gullies (Li et al., 2012).

Assigning an age to a terrace riser is difficult. Dating the surfaces of adjacent terraces can only provide upper and lower bounds for the age of the riser, resulting in large intervals of possible values of the fault slip rate, especially when the age difference between adjacent terraces is large (Lasserre et al., 1999; Van Der Woerd et al., 2002; Mériaux et al., 2005; Ryerson et al., 2006; Cowgill, 2007; Mériaux et al., 2012).

In this paper we use high resolution digital topography from two different sources to characterize the shape of alluvial fans and incised valleys and better constrain the lateral offsets they record along the fault. By first looking at the shape of the overall fans instead of incision features we avoid the ambiguity of assigning the age of the surface of a terrace to a displaced valley or riser. In a second part of the paper we focus on a narrow valley, west of the village of Shanxili where a shutter ridge partially closes the val-

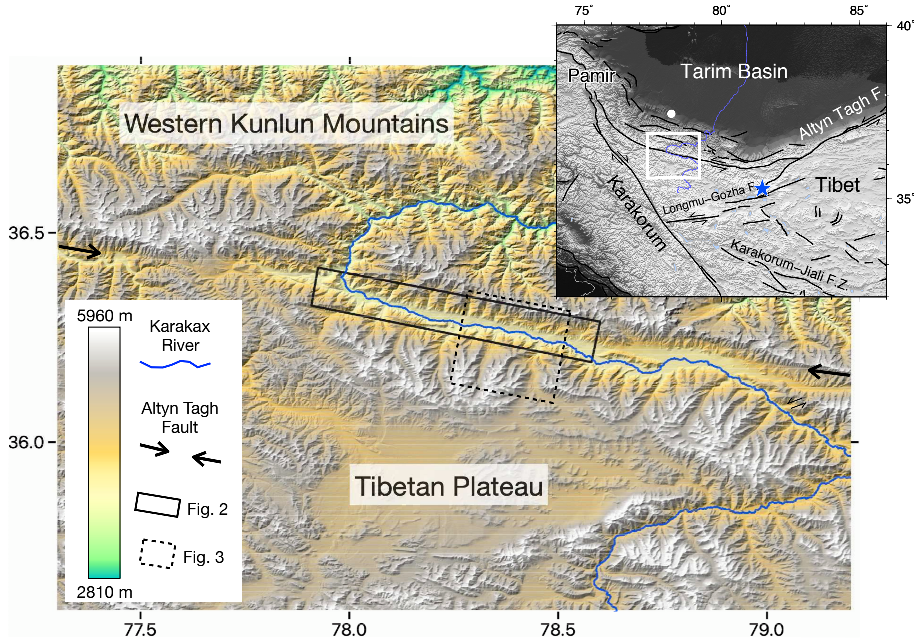

Figure 1. Topography of Western Kunlun and Tibetan Plateau area around study site. Solid line and dashed line boxes indicate areas covered by Figures 2 and 3, respectively. Inset: Simple tectonic map of Western Tibet. Solid lines depict active faults (Tapponnier & Molnar, 1977; Tapponnier et al., 2001). Blue star is location of Guliya Ice Cap. White dot shows location of Pishan terraces. White box indicates area covered by main panel. Background topography is rendered using SRTM data.

ley. There, the fault scarp is progressively exposed by the movement on the fault, resulting in a progression of its degradation along the fault strike. In the third part of the paper we combine the observed displacements with perviously published and newly obtained ages of terraces using cosmogenic radionuclide (CRN) samples from the upper terrace and optically simulated luminescence (OSL) samples from the inset terrace near Shanxili to estimate the long term slip-rate on the fault over the Holocene and the last glacial period. We finally discuss variable slip rate and variable erosion rate as possible causes of the non-linear relationship between the progressive degradation of the scarp and the cumulative displacement along the fault.

2 Geologic setting and morphology of the upper Karakax Valley

The Kunlun Shan extends from the Pamirs in the West to the Qaidam Basin in northeastern Tibet in the East. The western part of the range separates the western corner of the Tibetan plateau from the Tarim Basin to the north (Figure 1). With its highest summits exceeding 6000 meters along its southern edge, the elevation of the range gradually decreases to the north with an average slope of 1.9° over a distance of 120 km, reaching the top of the alluvial piedmont at the elevation of 1500 m. The upper Karakax Valley is a narrow valley oriented N110°E near the southern edge of the range formed by tectonic movement along the Altyn Tagh Fault. The valley is drained by the Karakax River, which veers to the north at the western end of the valley, down to the Tarim Basin where it merges with the Yurungkax into the Hotan River and eventually joins the Tarim River along the northern rim of the basin. Protected from the Asian monsoon and the Westerlies by the Karakorum and the Pamir mountains, the climate of the valley is arid and cold. Precipitation in the Western Kunlun mountains is heterogeneous, ranging be-

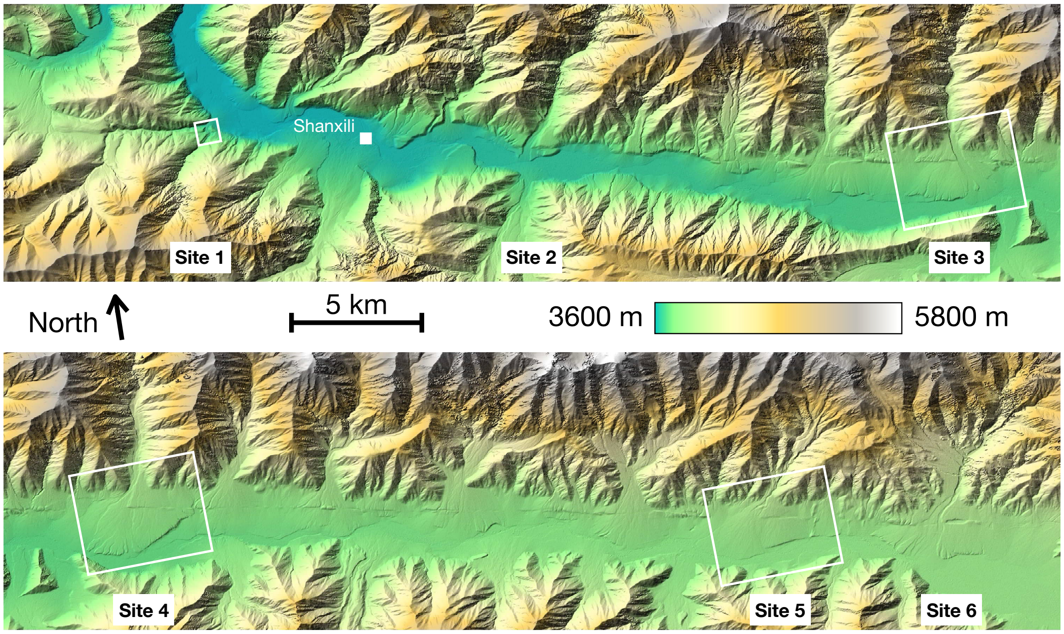

Figure 2. Shaded topography of upper Karakax Valley area from TanDEM-X digital elevation data (Hajnsek et al., 2014). Artificial illumination is from NW with elevation angle of 45°. Sites discussed in text are labeled by numbers. White boxes indicate detailed areas of sites 1, 3, 4, and 5 shown in Figures 4 and 5.

tween 70 mm/yr in the valleys to 350 mm/yr in the glaciated areas (Nakawo et al., 1990; J. Liu, 2011). Thompson et al. (1997) report accumulation of 200 mm (H_2O equivalent) per year over the Guliya Ice Cap in the eastern part of the western Kunlun range (Figure 1).

The valley has a narrow floor of ∼3.0 km in width carved by the floods of the Karakax River and covered with massive alluvial deposits mostly preserved along its northern side (Figure 2). The overall shape of the valley in the transverse direction is asymmetric with peaks up to 2300 m above the river level and steep slopes on the north side and more gentle slopes up to the mean elevation of the Plateau, 1500 m above the river level on the south side (Figure 3). The lower profile in Figure 3 represents the minimum incision profile achieved by tributaries of the Karakax River, north and south of the valley. Both the north and south side profiles have a typical shape with a lower section curved upward up to a knick-point, beyond which the profile slope is reduced. On the north side of the valley, the knick-point is located 1 km upstream from the Altyn Tagh Fault where it might have originated. Knick-points are often observed in profiles of rivers crossing faults with a vertical component of movement such as along this section of the Altyn Tagh Fault (Bull, 2007). On the south side profile however, the knick-point occurs 7 km south and 700 m above the present-day Karakax River. The knick-point location on the southern side of the valley seems to correspond to the lowest advance of glaciers on the north-facing slopes during the last glacial maximum. Satellite images and topography (Figure 1) show that above 4800 m in elevation on the southern side of the Karakax valley, river valleys are wider and filled with glacial till. This contrasts with the northern side of the valley where tributaries are steeply entrenched up to higher altitudes, glaciers are short with no evidence of significant advances to lower elevation.

The current course of the Karakax River follows the southern side of its valley, preserving the massive alluvial fans on its northern side (Figure 2). At several sites along the valley up to five levels of terraces can be recognized, attesting to changing conditions between periods of deposition and incision. As recognized in other arid environments,

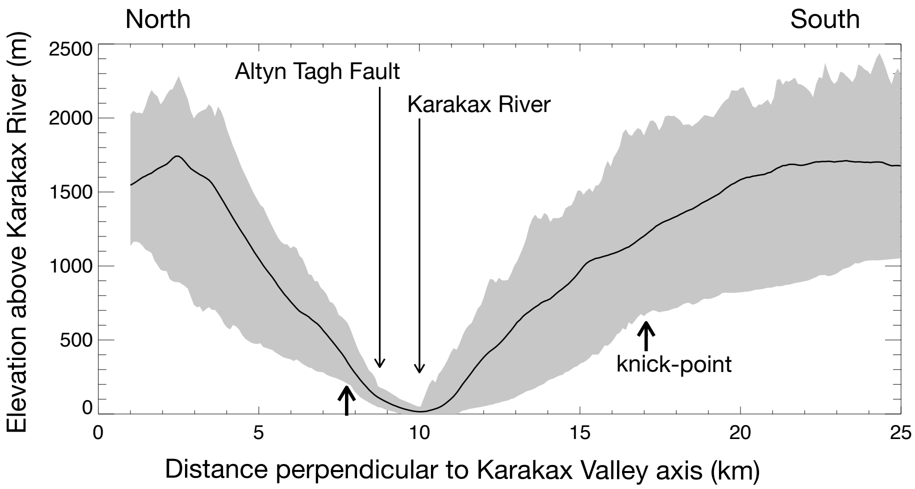

Figure 3. Mean topographic transect across Karakax Valley corresponding approximately to section shown in bottom panel of Figure 2 (see Figure 1 for location). Solid line is mean of 75 transect profiles distributed every 0.4 km over 30 km along valley. Elevation of each transect profile is referred to elevation of Karakax river at intersection point. Shaded area is bounded by profiles of minimum and maximum elevation within profiles set.

processes affecting the surface of abandoned alluvial terraces include aeolian deposition, salt weathering, desert varnish coating, the formation of desert pavement, and alluvial dissection (Bull, 1999). Except for channel incision, these processes tend to reduce the roughness of the surfaces with age. Farr and Chadwick (1996) used radar images acquired during the NASA SIR-C mission over the Karakax Valley to identify terraces at various stages of evolution. Using radar backscatter intensity as a proxy for age, they could distinguish three levels of terraces in the Valley. By comparing these observations with radar signatures of terraces in Death Valley in the southwestern United States the authors suggested that the upper terrace in the Karakax Valley was emplaced during the Eemian interglacial period, which began ∼125 kyr ago. This inference was later confirmed with the first age determination of the surface using cosmogenic radionuclides (Ryerson et al., 1999). Below we report new results based on CRN and OSL samples that place additional constraints on the ages of alluvial surfaces in the valley.

3 Digital topography data analysis

We use two digital elevation models (DEM) to characterize the shape of alluvial structures in the Karakax Valley. First we use the TanDEM-X DEM (Hajnsek et al., 2014) covering the entire section of the valley discussed in this paper, and second, a DEM generated from Pleiades tri-stereo images (Centre National d'Etudes Spatiales, 2016) over Site 1 for a detailed analysis of scarp degradation using a diffusion model. The TanDEM-X data obtained from the German Aerospace Center (DLR) correspond to the High Resolution Terrain Elevation, level-3 (HRTE-3) model specifications of 12 m posting and 2 m relative height accuracy for flat terrain (Hajnsek et al., 2014). These specifications allowed us to define the shape of alluvial structures and estimate their lateral displacement with unprecedented precision. The Pleiades images were processed using the AMES Stereo Pipeline (ASP) software (Beyer et al., 2018) into a 1 m posting DEM. The actual spatial resolution of the map is not quite 1 meter because of the size of the correlation window used by the ASP software but is sufficient to constrain scarp slopes of up to 40° over the height of the scarps we surveyed (Table 1). Given the angle of repose of colluvium of 35°, these specifications are adequate to perform degradation analysis of terrace risers and fault scarps in the Karakax Valley.

3.1 Offset of the Eemian terrace

The upper terrace along the north side of the Karakax River is characterized by a series of alluvial fans at the mouth of each tributary valley, with radii of ∼2 km and average radial slopes of 4.2-4.9° (Figure 2). At sites 3, 4, 5, and 6 the conical shape of the fans is conspicuous in the shaded topography and all fans appear to be incised by broad channels in various ways with the formation of cut terraces and the deposition of smaller units at lower levels (Figures 2 and 4). The surface trace of the Altyn Tagh Fault is clearly visible in the upper half of the fans as a straight feature parallel to the axis of the Karakax Valley. The complex assemblage of fan structures and inset terraces has been cut and offset by repeated displacement along the Altyn Tagh Fault.

We selected three alluvial fans where the upper terrace is well preserved and can be used to estimate the horizontal and vertical displacements on the fault since their emplacement (Figure 4). At Site 3 the conical surface of the fan is entirely preserved except where a ∼300 m-wide channel has incised its surface down ∼10 m on the eastern side of the fan. At sites 4 and 5, a large part of each fan's upper surface has been removed by incision and subsequent channel widening and deposition on their western sides. Only the preserved part of the upper surface of the fans can be used for estimating the offsets at those sites. For each of these 3 fans we reconstruct the lateral and vertical shifts on the fault using a four-step procedure (Figure 4): (1) The elevation of points within 100 m from the fault are projected in a profile as a function of distance along the fault. (2) The surface slope perpendicular to the fault is removed by using a slanted projection direction, parallel to the fan surface slope. (3) The vertical throw on the fault is restored by aligning the elevation of the apexes of the conical shape of the profiles on both sides of the fault. (4) Finally the horizontal shift is restored by aligning the parts of the profiles corresponding to the upper surface. The restored offset of the upper surface at these sites is ∼300± 20 m with a south side down vertical throw of ∼12-15 m. The confidence interval of ±20 m of lateral shift estimates is based on the dispersion of the profile points in the horizontal direction parallel to fault strike along fans lateral slopes. Assuming that the emplacement of the bulk of the fans occurs on a relatively short period of time, these values can be associated with the exposure age of the upper terrace determined using the cosmogenic radionuclide method without ambiguity (Mériaux et al., 2012, e.g.). The vertical movement along the fault is generally south side down but can vary depending on the local direction of the fault trace, which in places forms compressional and releasing bends. At Site 6 for example, a 700 m-long pull apart structure has developed in the upper terrace as the result of the sinistral slip on fault segments forming a left step (Figure 2). The development of the pull-apart modified the shape of the upper surface at this site, making it difficult to restore its shape using the method used at sites 3-5.

Note that features incising the upper surface of the fans appear laterally offset by a lesser amount, consistent with a younger age of formation. For example at Site 3, the clear-cut incised channel on the eastern slope of the fan appears to be left-laterally offset by ∼80±10 m (Figure 4). Similarly, the main risers incising the upper surface at Site 4 and 5 appear to be offset by 200-240 m and therefore must have been formed some time after the deposition of the terrace they bound (Figure 4).

3.2 Offset river channel and inset terrace at Site 1

Unlike the other sites discussed in this paper, Site 1 is located on the southern side and western end of the Karakax Valley where the river veers to the north and begins its descent towards the Tarim Basin. At this site, a tributary of the Karakax River has dug a 200 m-wide valley in a flat terrace, dipping ∼9.8° to the North, and lies ∼75 m above the Karakax River flood plain (Figure 5). The upper terrace and the incised channel have been cut and laterally displaced by slip on the Altyn Tagh Fault. The fault displacement has brought a piece of the upper terrace (T3) into the incised channel, forming a shutter ridge partly damming the valley (Figure 5). The tributary has deposited an inset ter-

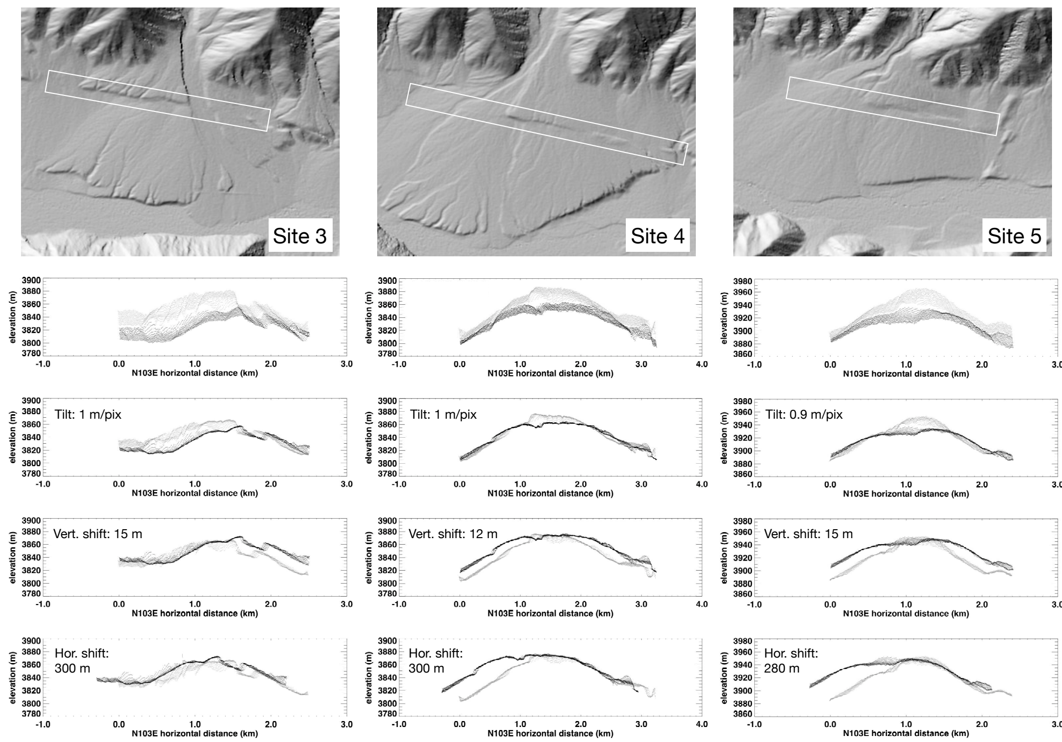

Figure 4. Offset fan surface at sites 3 (left), 4 (center), and 5 (right). For each site, top image shows shaded topography of alluvial fan from TanDEM-X data with illumination from NW. White box represents area used in elevation profiles. Profiles show elevation vs distance along fault strike. Black and grey points correspond to southern and northern sides of fault, respectively. Top is raw profile, second from top is profile with slanted projection parallel to fan surface slope, third from top is profile after restoration of fault vertical throw to align apex of profiles between two sides of fault, and bottom is profile after restoration of left-lateral shift to align older surface (eastern slope) between two sides of fault.

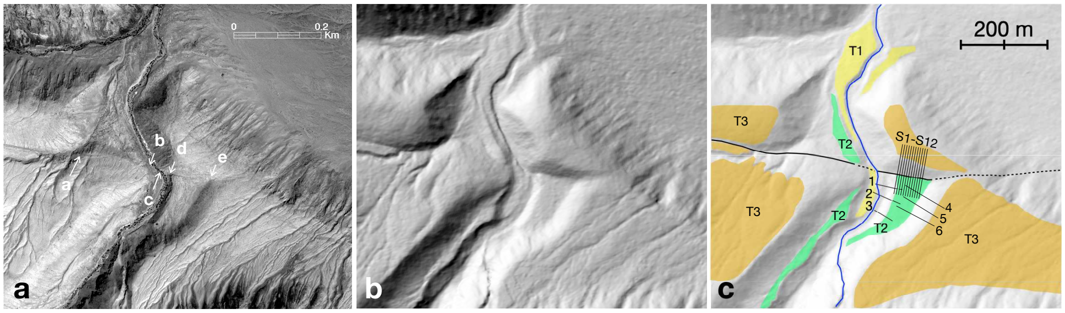

Figure 5. Detailed view of Site 1. a: High resolution ortho-rectified Pleiades image. White arrows with labels point to piercing points of offset morphological features discussed in text. b: Shaded DEM obtained from Pleiades images. c: Map of main alluvial terraces at Site 1. Solid lines indicate location of profiles used for degradation analysis (Figure 6, Table 1). Note sun illumination from SE direction in satellite image (a) and NW direction in shaded DEM (b, c).

race (T2), which is well preserved on the right-hand side of the river, south of the fault. The lateral offset of the river channel is between 118±5 m (east side wall offset between arrows c and e in Figure 5a) and 165±5 m (west side wall offset between arrows a and b in Figure 5a). However, the actual value of the channel offset may lie between these extreme values because the channel walls on both sides, north of the fault seem to have been eroded by water flow in a channel coming from the west at point *a* and in the main river channel at point *d*, thus increasing the apparent maximum offset between piercing points *a* and *b* and decreasing the apparent minimum offset between piercing points *c* and *e* (Figure 5a). Finally, the terrace riser below the inset terrace (T2) appears to have a minimum offset of 23±2 m across the fault, between piercing points *c* and *d* (Figure 5a).

3.3 Progressive exposure and degradation of fault scarp along shutter ridge

A remarkable feature of the evolution of this site over time is the gradual exposure of the fault scarp as the shutter ridge is being displaced into the channel by fault movement. This particular setting requires that the degradation of the exposed fault scarp due to surface erosion must increase toward the west between piercing points *e* and *d* (Figure 5) because the western part of this section has been exposed to erosion a longer time than its eastern part. To test this hypothesis we estimate the scarp degradation along the exposed fault scarp as a function of distance along the fault. Scarp erosion in arid environment has long been studied using a diffusive mass transport models (Wallace, 1977; Nash, 1980; Andrews & Hanks, 1985; Avouac, 1993; Hilley et al., 2010, e.g.,). Following a similar approach, we assume here that the fault scarps and terrace risers start to collapse soon after their formation to achieve a slope at the angle of repose of coarse colluvium. This phase takes a relatively short time compared to the diffusion period of several thousands of years that follows (Wallace, 1977). The evolution of the scarps during the diffusion period is modeled using a convolution with a Gaussian curve of width $\sqrt{2kt}$, where t is the time since the formation of the scarp and k is the mass diffusivity constant of the terrace material under the prevailing climatic conditions. The value of kt represents the degradation coefficient of the scarp and its age t can be estimated if the diffusivity constant k is calibrated. Under arid conditions in the western United States and Central Asia, values ranging from 1 to 5 m^2/kyr have been estimated for the mass diffusivity constant (Avouac, 1993).

Using the 1 m-posting DEM generated using the Pleiades tri-stereo images, we extract elevations profiles of fault scarps and terrace risers and estimate their degradation coefficients as follows. We first adjust a gaussian curve plus a constant term by non-linear least squares regression of the slope profile derived from the elevation profile (Figure 6a). This step defines the center of symmetry of the scarp, the slope of the terraces on both sides of the scarp, and the vertical separation between them. Using these defined parameters, we construct a synthetic scarp profile representing the shape of the scarp after its collapse into a colluvial wedge with an angle of repose of 35° (Figure 6b). Two straight segments are parallel to the slope of the adjacent terraces and the middle segment is parallel to the slope of the colluvial wedge. We then iteratively convolve the synthetic scarp curve with a series of gaussian functions, varying their width within a range of possible values, and compute the quadratic misfit between the convolved curve and the observed profile (Figure 6d). Finally we select the optimal degradation coefficient kt that minimizes the misfit (Figure 6b, c). It is often observed that the lower part of scarp profiles is modified by the erosion of a lateral channel or by the deposition of sediments at their base, leading to the loss of symmetry of the profile. We therefore compute the misfit between the modeled and the observed profiles using only the upper half of the profile. The erosion coefficient is then constrained by the curvature of the upper part of the scarp and is not influenced by the modified base of the scarp profile. We adopt this approach at Site 1 because the profiles of both risers below terraces T2 and T3 and the exposed fault scarp show evidence of erosion or channel incision at their base (Figures S1 and S2).

We extracted a series of twelve elevation profiles separated by 5 m across the exposed fault scarp at Site 1 (S1-S12 in Figure 5). The method described above is applied to each scarp profile to estimate its degradation coefficient (Table 1 and Figures S1 and S2). Figure 10 shows the variations of the optimal values of kt as a function of the horizontal distance along the fault. The degradation increases westward along the scarp, which is consistent with a westward movement of the northern side with respect to the southern side. Between 10 m and 65 m along the fault scarp, its degradation coefficient varies from 22 to 74 m^2, giving an average degradation rate of 0.94 m^2/m (Figure 10). This value means that if the mass diffusivity constant was 1 m^2/ka for the colluvium in the Karakax Valley during the last 100 ka, the average slip-rate of the fault would be 1.06 mm/yr. Estimating the actual fault slip-rate requires a calibration of the mass diffusivity constant.

It is interesting to note that the rate of degradation per meter along the fault is not constant. Figure 10 shows two periods of low degradation rate along the 10-20 m and 35-65 m segments, separated by a period of higher degradation rate along the 20-35 m segment. This non-linear relationship could be the result of a variable slip-rate on the fault during the gradual emplacement of the shutter ridge or due to variations of the mass diffusivity with time through this period. We will discuss the implications of these two non-exclusive options together with constraints on the mean diffusivity constant using surface age estimates in a later section.

3.4 Degradation of terrace risers at Site 1

Site 1 main alluvial surfaces are the upper terrace (T3) and the inset terrace (T2). A lower terrace (T1) exists in places along the stream flowing from the south into the Karakax River but it is discontinuous and narrow. Both terraces have been incised by the stream, forming steep risers on the eastern side of the valley (Figure 5). We extracted six elevation profiles across the terrace risers from the Pleiades DEM and assessed the degree of degradation using the same method as for the fault scarp (Table 1). The lower riser below the T2 terrace is close to the present location of the stream and may have been reshaped during storms when the stream flow increased. This may explain the anomalously low degradation coefficients for profile 3 compared to profiles 1 and 2 (Table 1). To calibrate the mass diffusivity constant we use the largest degradation coefficient to associate with the time of deposition of the terrace. We therefore take the value of 15.6 m^2 to characterize the degradation of the lower riser at Site 1. The values of degradation coefficients for the higher riser between terraces T2 and T3 range from 59 to 75.0 m^2. Similar to the lower riser, the higher riser may have experienced episodes of reshaping when the stream was still flowing along its base before being permanently abandoned

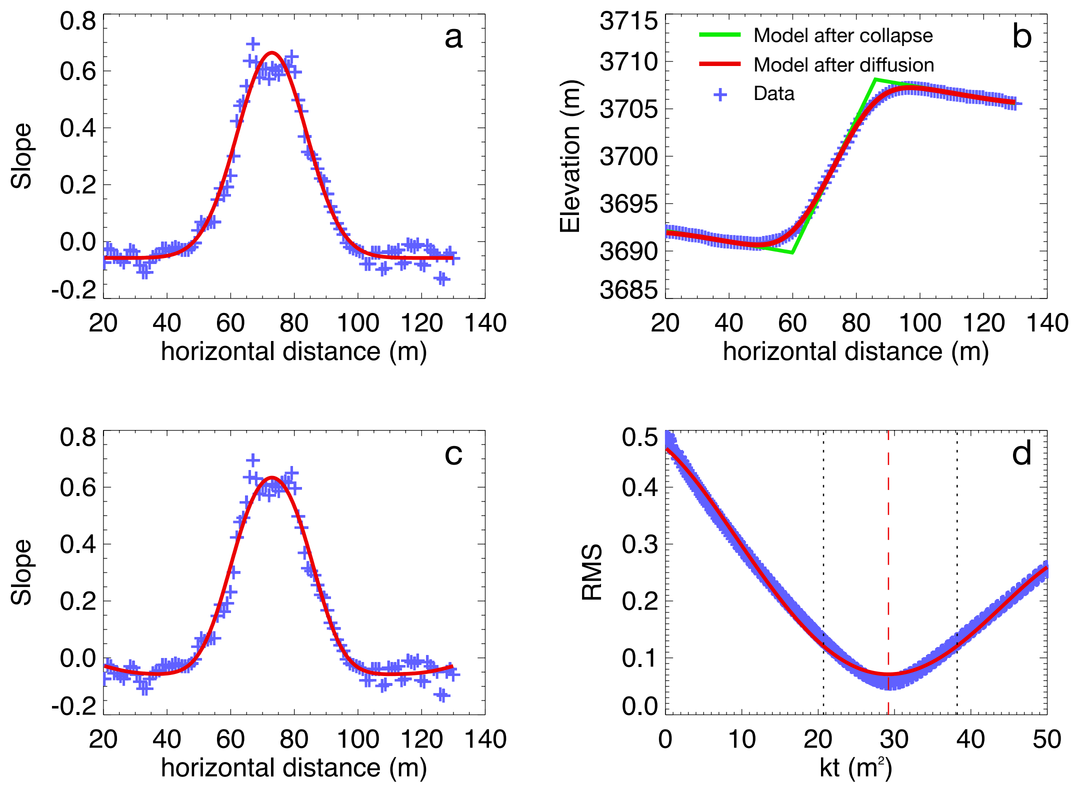

Figure 6. Example of observed and modeled profiles of scarp across Altyn Tagh Fault (S10 in Figure 5). a: Simple Gauss plus constant function (red curve) fit to observed slope profile (blue symbols). b: Observed elevation data for profile S-10 (blue symbols). Green curve is synthetic profile after formation of colluvial wedge. Red curve is best fit model after erosion by mass diffusion. c: Observed (blue symbols) and best fit model (red curve) slope profiles. d: RMS misfit between observed and modeled elevation profiles for explored range of kt values. Red curve is polynomial fit to data points to define minimum.

Profile Number	Distance (m)	Scarp height (m)	kT (m^2)	RMS (m)	Type
		Fault scarp			
S1	65	27.89	74.0 +9.0/-8.5	0.24	Fault scarp
S2	60	27.97	73.0 +8.5/-8.0	0.17	Fault scarp
S3	55	27.84	69.0 +8.5/-8.0	0.15	Fault scarp
S4	50	27.84	69.0 +8.5/-8.0	0.17	Fault scarp
S5	45	26.51	65.0 +8.5/-8.5	0.18	Fault scarp
S6	40	24.60	62.0 +9.0/-8.0	0.16	Fault scarp
S7	35	23.70	62.0 +8.5/-8.5	0.17	Fault scarp
S8	30	22.22	57.0 +9.5/-8.5	0.20	Fault scarp
S9	25	20.27	40.0 +7.5/-6.5	0.16	Fault scarp
S10	20	19.77	29.2 +4.5/-4.2	0.07	Fault scarp
S11	15	19.80	24.6 +4.5/-4.3	0.10	Fault scarp
S12	10	19.45	22.2 +4.7/-4.4	0.13	Fault scarp
		Terrace risers			
R1	-	10.21	15.6 +3.6/-3.2	0.09	T1/T2 Riser
R2	-	9.68	11.5 +5.7/-4.1	0.29	T1/T2 Riser
R3	-	11.20	6.8 +3.7/-2.6	0.20	T1/T2 Riser
R4	-	18.96	71.0 +13.0/-11.5	0.36	T2/T3 Riser
R5	-	22.30	75.0 +11.0/-10.0	0.22	T2/T3 Riser
R6	-	22.75	59.0 +9.0/-8.5	0.21	T2/T3 Riser

Table 1. Scarp degradation analysis using diffusion model at Site 1. Profile numbers refer to labels in Figure 5. Distance is westward distance along fault scarp from riser T2-T3.

after the deposition of terrace T2. Thus, we choose the largest value of 75 m^2 to represent the degradation coefficient of the riser between T2 and T3 at Site 1.

4 Age of Quaternary surfaces in the Karakax Valley

Studies conducting direct age estimates of the Karakax Valley terraces started in the mid 1990s and only partial results have been published so far (Ryerson et al., 1999; Li et al., 2008, 2012; Gong et al., 2017). Here we report on new analyses of samples collected at Site 1 and Site 4 along the valley (Figure 2). At Site 1, fine grain fluvial sediments collected in an inset terrace of the tributary valley are analyzed using the OSL method (Aitken, 1985; Wintle, 1997; Aitken, 1998; Duller, 2004). At Site 4, quartz-bearing cobbles and pebbles were collected at the surface of terraces and in depth-profiles in the shallow (∼2 m) subsurface (Ryerson et al., 1999). Here we present new results obtained with surface samples only.

4.1 Age of terraces at Site 4 using cosmogenic radionuclide dating

^{10}Be cosmic-ray exposure model ages were determined for 28 surface samples from terraces at Site 4 (Figure 7). All of the ^{10}Be measurements were made at the Center for Accelerator Mass Spectrometry at Lawrence Livermore National Laboratory following chemical separation methods described by Kohl and Nishiizumi (1992). Hand size cobbles and fragments from boulders with dimensions up to 0.5 m in diameter, similar to those in the active channel, were collected from surfaces T2 and T2”. The surfaces above these levels, T3 and T4, are essentially smooth and covered with a 5-20 cm-thick layer of silt, which appears to be a mixture of shattered cobbles and loess, partially paved with small quartz pebbles (∼1 cm in diameter). Given the absence of cobbles on the T3 and T4 surfaces, quartz pebbles were collected from a number of ∼1 m diameter, roughly circular patches on the surfaces. The collection of pebbles within each patch constituted a single sample for CRN dating; individual pebbles were too small for dating. Subsurface observations obtained by refreshing terrace risers indicated that cobbles, similar to those on the surface of T2 and T2" are present at depth and are progressively shattered closer to the surface. The pebbles on the surface are interpreted to represent the remnants of these shattered cobbles as the result of salt weathering (Farr & Chadwick, 1996).

The ^{10}Be concentrations were converted to model ages using the CRONUS online calculator version 3 (https://hess.ess.washington.edu/), which accounts for the various exposure constraints and incorporates a number of production rate scaling models (Balco et al., 2008; Phillips et al., 2016, cf). Numerous scaling frameworks have been proposed to correct for latitude, elevation, atmospheric pressure anomalies, dipole and non-dipole geomagnetic field changes, and solar modulation, etc... (Borchers et al., 2016, cf). The current online version of the CRONUS calculator includes the original model by Lal (1991), further developed by Stone (2000) (referred to as St), a version of the St model incorporating paleomagnetic corrections described in Nishiizumi et al. (1989) (referred to as Lm) and a model employing analytical approximations fit to nuclear-physics simulations of the cosmic-ray cascade (referred to as LSDn) (Lifton et al., 2014).

Chauvenet's criterion, a well established statistical method to define clusters and outliers in a sample set (Bevington & Robinson, 2002), was used to eliminate statistical outliers in the sample populations for T2", T3, and T4 surfaces (Mériaux et al., 2012) (Table 2). In addition to variations associated with the production rate scaling, CRN model ages may be influenced by the effects of sample inheritance, leading to an overestimation of the age, and surface erosion and shielding, resulting in an underestimation of the age. A preliminary analysis of the samples from depth-profiles at Site 4 indicated negligible inheritance (Ryerson et al., 1999). This is supported by the steep slopes and short drainages observed on the North side of the valley, suggesting a rapid exhumation and transport of the colluvium material before deposition (Figure 4). Furthermore, in a recent study Guilbaud et al. (2017) estimated that erosion rates on alluvial terraces along the northern piedmont of the Western Kunlun mountains near Pishan were low (<1.5 mm/ka) (Figure 1). Transient shielding by snow, eolian deposition of loess, and vegetation may also influence CNR model ages. The arid climate of the valley limits the amount of snow fall and the vegetation is essentially non existent on these alluvial fans. The Kunlun Mountains also offer a natural barrier to the flux of eolian sediments emanating from the Tarim Basin, as confirmed by the limited amount of loess in the mixed layer at the top of terraces (Farr & Chadwick, 1996). Based on these arguments, the CRN model ages we present here assume that the effects of inheritance, erosion, and shielding are small and lie within uncertainty defined by analytical error of CRN concentration and scaling models.

Overall, the ages of surface samples correlate with surface morphology and position relative to the active channel with terraces T2 and T2" yielding younger ages than those of T3 and T4 (Figure 7). The model ages vary depending upon the choice of production rate scaling model, however, and the disparity among models becomes greater with nuclide concentration/age. The mean age and standard deviation for the T2" samples (minus statistical outliers) derived from the production rate scaling models St, Lm and LSDn models are the same within error, 11.3 ± 1.8 ka, 11.7 ± 1.5 ka and 11.7 ± 1.3 ka, respectively. However, the highest surface, T4, yields more disparate mean ages of 134.3 ± 9.1 ka, 120.4 ± 7.5 ka, and 112.9 ± 6.5 ka, respectively, for St, Lm and LSDn scaling models (Figure 8). While these disparate ages indicate that there are still unresolved difficulties in modeling cosmogenic nuclide production and the calibration of production rates (Borchers et al., 2016, cf), the range of ages correlates well with the transition from δ^{18}O isotopic stages MIS-6 to MIS-5 (Figure 8). Alluvial fan deposition during the presumably dry Stage MIS-6 glaciation is unlikely, thus we argue that the younger

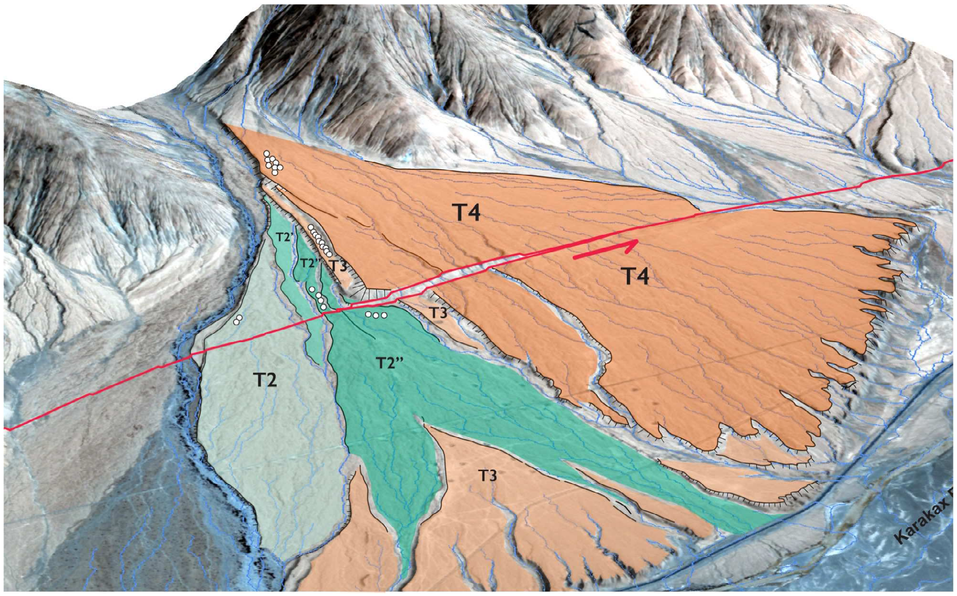

Figure 7. Composite 3D scene of Site 4 assembled by draping Pleiades image over Pleiades-based DEM. Terrace surfaces are numbered and shaded as a function of increasing age and elevation from river bed (T2: pale green, T2": green, T3: pale orange and T4: orange). White circles correspond to general locations of amalgamated samples for CRN surface exposure dating.

Lm and LSDn ages obtained from the more recent production rate scaling models best represent the age of T4 fan deposition at ∼115 ka, equivalent to $\delta^{18}O$ isotopic stage MIS-5e. The ages for T3 obtained from the St, Lm and LSDn scaling models are 110.2 ± 3.9 ka, 106.4 ± 1.3 ka and 95.6 ± 2.8 ka, respectively. Using similar logic, the LSDn age of ∼96 ka best represents the age of T3 surface emplacement.

The CRN model ages indicate 2 main phases of aggradation of the imbricated alluvial fan at site 4 (Figure 8). The majority of the model ages of surface samples on the lower levels, T2 and T2", are younger than the Last Glacial Maximum (LGM at ∼19ka). Moreover, the final distribution of CRN model ages for surface samples is younger than 15 ka, which indicates that the lower level of the fan formed during the warm post-glacial period of increased run-off that followed the dry glacial age, as found in several other regions of Tibet and central Asia (Mériaux et al., 2012; Van Der Woerd et al., 1998, i.e.,). The upper levels T4 and T3 yield CRN model ages ranging from ∼115 ka to ∼100 ka, respectively and coincide with the $\delta^{18}O$ isotopic stages MIS-5e and -5c (Figure 8) consistent with the alluvial fan complex deposition during the Eemian interglacial, which ended ∼115 ka ago (Dahl-Jensen et al., 2013).

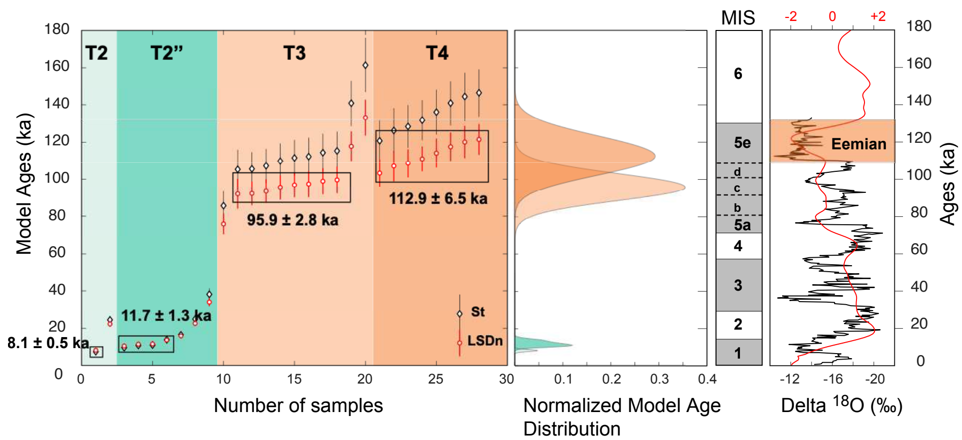

Figure 8. Left: CRN model ages of surface samples collected on T2, T2”, T3 and T4 at Site 4 (T2: pale green, T2”: green, T3: pale orange and T4: orange). Only model ages determined using the St and LSDn production scaling schemes in CRONUS, with outliers eliminated using Chauvenet’s Criteria are shown. As described in the text, the LSDn ages are preferred here. The error bars include both analytical and model uncertainty. The boxes include the LSDn model ages minus the statistically defined outliers. The mean age and standard deviations of the LSDn cluster are also indicated. Right: Comparison of the normalized model age distribution for the various surfaces (color code is the same as in the left-hand panel) with SPECMAP marine isotope stages (Imbrie et al., 1984; Winograd et al., 1997) in red, $\delta^{18}O$ changes of the Guliya ice-cap core (Thompson et al., 1997). The age distributions for T3 and T4 surface correlate well with MIS 5e and MIS 5c, while T2 and T2” distributions are consistent with deposition of these surfaces after the LGM.

Table 2. CRN model ages for different production scaling models

Scaling Model	St		Lm		LSDn	
	Age (yr)	Error	Age (yr)	Error	Age (yr)	Error
T2						
KR4-1	7468	638	8060	659	8166	550
KR4-9*	24496	2113	23247	1918	22295	1518
T2"						
KR4-2	9610	798	10313	817	10411	668
KR4-5	10745	1238	11336	1276	11359	1165
KR4-3	10944	1101	11488	1120	11493	986
KR4-6	13735	1143	13811	1097	13595	876
KR4-8*	16463	1465	16267	1389	15830	1134
KR4-7*	24921	2115	23621	1915	22610	1500
KR4-4*	38189	3196	35699	2849	34087	2204
Average (ka)	**11.3**		**11.7**		**11.7**	
Std-Dev (ka)	**1.8**		**1.5**		**1.3**	
T3						
KR4-T1E*	85988	7718	79980	6876	75948	5450
KR4-T1J	105265	10686	96878	9500	92308	7912
KR4-T1G	105533	9187	97094	8065	92512	6300
KR4-T1C	107182	9215	98436	8065	93734	6252
KR4-T1I	109797	9464	100586	8262	95633	6402
KR4-T1D	111581	9619	102044	8382	96912	6486
KR4-T1K	112293	10061	102620	8792	97420	6936
KR4-T1H	114387	10123	104283	8814	98935	6905
KR4-T1F	115352	10312	105039	8975	99639	7065
KR4-T1B*	140798	12276	125666	10429	117794	7977
KR4-T1Kb*	161371	14654	143887	12471	133085	9577
Average (ka)	**110.2**		**100.9**		**95.9**	
Std-Dev (ka)	**3.9**		**3.2**		**2.8**	
T4						
KR4-STO-E	120741	10878	109337	9418	103288	7404
KR4-STO-C	126232	11907	113814	10300	107083	8225
KR4-STO-F	128396	11428	115561	9818	108624	7626
KR4-STO-I	131748	10765	118313	9148	110999	6742
KR4-STO-J	136040	11966	121743	10205	114107	7846
KR4-STO-H	140862	11974	125701	10145	117552	7630
KR4-STO-B	144336	13054	128638	11109	120067	8615
KR4-STO-G	146350	12790	130360	10843	121448	8245
Average (ka)	**134.3**		**120.4**		**112.9**	
Std-Dev (ka)	**9.1**		**7.5**		**6.5**	

* Sample identified as a statistical outlier using Chauvent's Criteria.
Model ages were calculated using the CRONUS-Earth online cosmogenic nuclide calculator (https://hess.ess.washington.edu/). Errors on the model ages are calculated by propagating the analytical uncertainties together with a 7.9% error on the production rates (Stone, 2000; Borchers et al., 2016) and 0.86% uncertainties for the decay constants of ^{10}Be (Chmeleff et al., 2010; Korschinek et al., 2010).

4.2 Age of inset terrace emplacement using Optically Simulated Luminescence (OSL) method

Due to differences in lithology between the mountains north and south of the valley and the lack of time during our field visit, we did not collect samples for cosmogenic analysis at Site 1. Instead, we collected samples in a fine grain layer of the inset terrace (T2) for OSL analysis (Figure 9). The inset terrace is a 10 m-thick terrace deposited in the 100-200 m-wide valley entrenched in the upper terrace (T3). Its flat surface is dipping $\sim$4.8° to the north and abuts the fault scarp against the shutter ridge (Figure 5). The inset terrace is formed mostly of medium coarse colluvium of debris flow origin. Approximately 6 m from the top of the terrace, a $\sim$50 cm-thick sequence of alternating fine sand and silt narrow beds has been deposited. This section of the stratigraphic sequence was well exposed due to the erosion of the riser in a meander of the stream flowing at its base (Figure 9). Fist-size silt blocks were collected $\sim$50 cm into the wall of the riser and kept away from light in sealed aluminum boxes.

A cubic centimeter volume of the fine grains was extracted from the center of each of the two sample blocks, hereafter referred to as J1232 and J1233 samples, and prepared using a standard preparation procedure (Porat et al., 2015) (see Supplementary Information for a full description of the sample preparation and measurement procedure).

The emission of K-feldspar multi-grain aliquots from sample J1232 and single grains from sample J1233 was stimulated using a post-infrared infrared stimulated luminescence (pIRIR) protocol (Buylaert et al., 2009). The emission of quartz aliquots of the J1232 sample was stimulated using blue LEDs. All measurements were performed on a Risø TL/OSL-DA-20 automated luminescence reader. The geologic dose rates of the samples were determined by estimating the concentration of U, Th, and K elements using spectrometry methods and corrected for cosmic ray contributions (Table 3). A description of the geologic dose rate determination can be found in the Supplementary Materials. The results are summarized in Table 3. The equivalent dose, determined using the central age model (Galbraith et al., 1999) for K-feldspar from both samples, are in excellent agreement (within 1σ) and exhibit low overdispersion (Figure 9, Table 3). After normalization by the total geological dose rate, the equivalent dose values lead to ages of 9.49$\pm$0.89 ka and 8.46$\pm$0.46 ka for samples J1232 and J1233, respectively.

The equivalent dose distribution for the quartz aliquots from sample J1232 is skewed towards lower values because of the presence of unstable components within the measured signal (see discussion in Supplementary Information). We used the maximum age model, as implemented by (Burow, 2019) to estimate the equivalent dose of 35.4$\pm$6.5 Gy yielding an age of 7.91$\pm$1.5 ka after normalization by the geologic dose rate. This age is less precise than the age derived from K-feldspar samples but is internally consistent within 1 σ (Table 3). Finally, the narrow confinement imposed by the 200-wide valley and the absence of sedimentological evidence for paleo-surfaces in the 10 m-thick section of the terrace argue for a rapid emplacement of the inset terrace at this site.

In the following, we will use the weighted mean of 8.8$\pm$0.6 ka of the two K-feldspar ages above for the age of Terrace T2 at Site 1. This early Holocene age corresponds to the end of the 7-15 ka warm period defined by the δ^{18}O variations observed in the ice core from the Guliya Ice Cap (Thompson et al., 1997), located in the western Kunlun range, $\sim$330 km ESE of Site 1 (Figure 1).

5 Discussion: Glacial and post-glacial slip-rate on the Karakax section of the Altyn Tagh Fault

The ages of the alluvial terraces provided by the OSL and CRN dating methods place constraints on the slip-rate on the Altyn Tagh fault over the last glacial and post-glacial periods. The 300$\pm$20 m lateral offset of the upper surface of the alluvial fans at sites 3, 4, and 5 integrates the fault movement since the deposition of the units at the

Table 3. Luminescence results for samples collected at Latitude 36.3609°N, Longitude 77.9848°E, depth 6 m.

Lab code	Field code	Mineral	K (%)	Th (ppm)	U (ppm)	Grain size (μm)	Total dose-rate (Gy/ka)[a]	Equivalent dose (Gy)	Age (ka)
J1232	K2-TL-1	K-feldspar	2.5	14.1	4.43	125 - 175	5.18± 0.24	49.2 ± 4.0[2]	9.49 ± 0.89
J1232	K2-TL-1	Quartz	2.5	14.1	4.43	63 - 100	4.47± 0.20	35.4 ± 6.5[3]	7.91 ± 1.50
J1233	K2-TL-2	K-feldspar	2.2	13.8	3.83	175 - 200	4.76± 0.19	40.3 ± 1.5[2]	8.46 ± 0.46

[1]Calculated using DRAC v1.2 (Durcan et al., 2015), using the factors of Liritzis et al. (2013); Huntley and Baril (1997); Brennan et al. (1991); Guérin et al. (2012); Bell (1979).
[2]Central age model of Galbraith et al. (1999) used. Calculated overdispersion of 10 and 17% for J1232 and J1233, respectively.
[3]Maximum age model (Burow, 2019) used assuming an overdispersion of 15%.

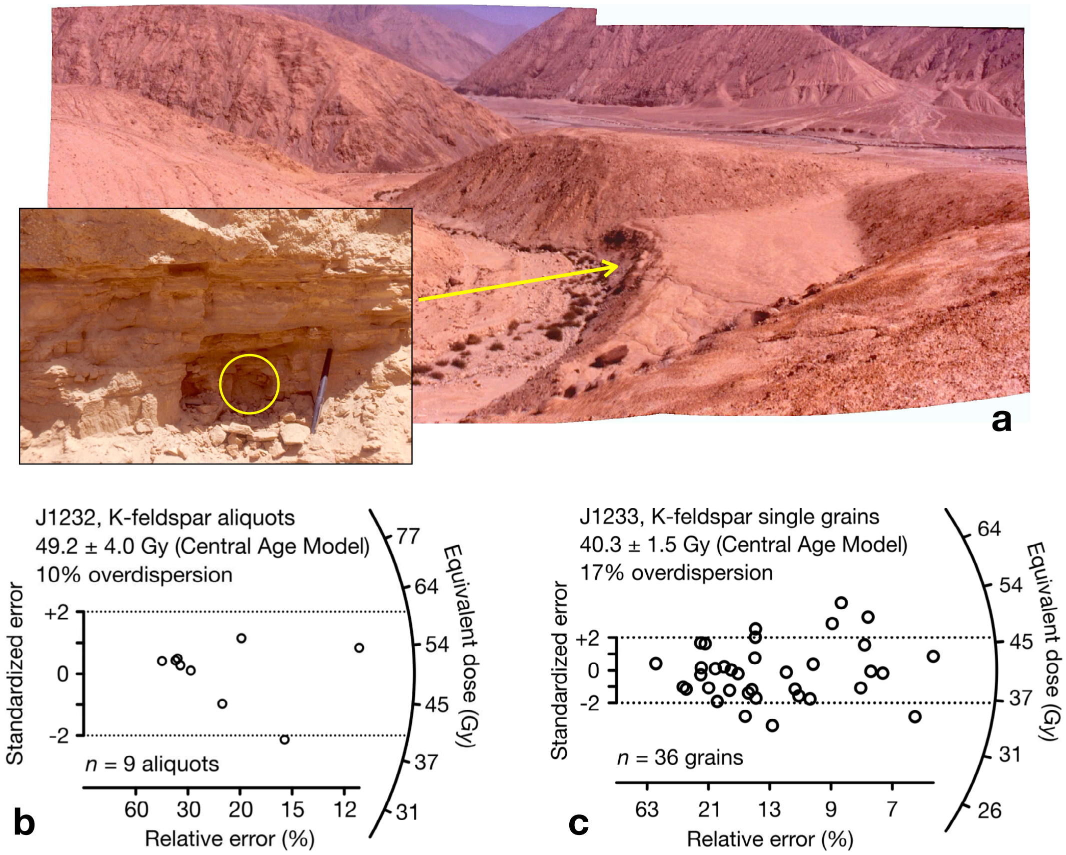

Figure 9. a. Field picture of Site 1, looking North from edge of upper terrace. Inset shows close-up view of sedimentary series where OSL samples were collected (circle) with pen for scale. b, c. Radial plots showing equivalent dose distributions of samples J232 (b) and J233 (c).

end of the Eemian. The inferred age of 115±7 ka for the upper terrace at Site 4 leads to an average slip rate of 2.6±0.3 mm/yr over this time period.

Inferences about the fault slip rate at Site 1 come from different lines of observation and kinematic reconstruction of the emplacement of the shutter ridge. The most direct slip rate estimate is obtained by dividing the minimum lateral offset of riser T1-T2 by the age of Terrace T2. This yields a minimum slip-rate of 23±2 m in 8.8±0.6 ka, or 2.6±0.5 mm/yr. This value matches the value obtained for the average slip-rate over the last 115 ka, consistent with a constant slip-rate through time.

However, the progressive exposure of the fault scarp at Site 1 provides more information about the slip-rate on the fault and its evolution in time over part of the last glacial period. Here, the age of Terrace T2 can be used to calibrate the average mass diffusivity constant over the Holocene. The diffusion model indicates a degradation coefficient kt=15.6 m^2 for the T1-T2 riser. If the formation of the riser occurred shortly after the deposition of the Holocene terrace, a minimum value of the mass diffusivity constant is k = 15.6 m^2/8.8 ka = 1.7 m^2/ka. Assuming that this value of k remained constant over the last glacial period, a slip history of the fault can be inferred from the evolution of the fault scarp degradation as a function of distance along the fault (Figure 10a). Under this assumption the fault slip-rate appears to have varied in the second half of the last glaciation with periods of faster slip (3-4 mm/yr) during the 12-17 kyr and 35-45 kyr intervals, slowing down to a sub-mm/yr rate between 20 and 32 kyr. This apparent surface slip-rate variation could be simply the result of earthquake clustering in time. Li et al. (2012) report clusters of small channel offsets on the nearby Sanxili-Yingfang

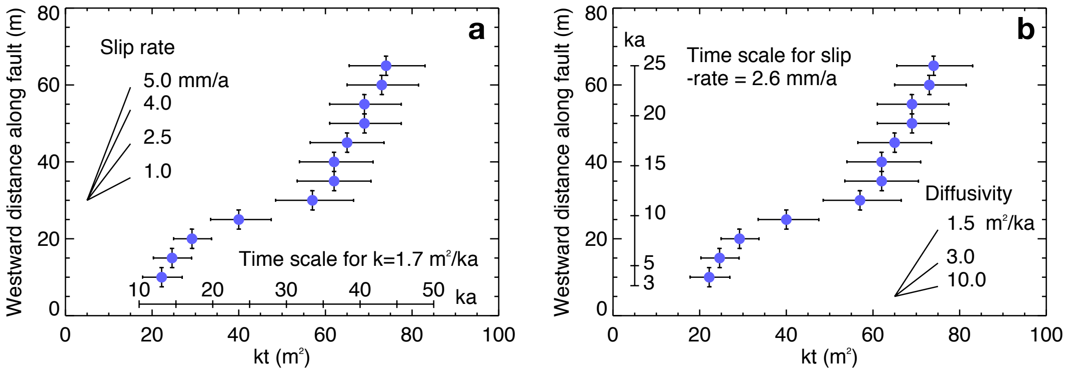

Figure 10. Two alternative interpretations of distance along fault vs scarp degradation relationship. For both a and b, origin of westward distance of profile is at intersection between fault trace and T2-T3 riser. a: If mass diffusivity is constant, graph shows variations of fault slip-rate through time. b: If slip-rate is constant, graph shows variations of mass diffusivity with time.

alluvial fan that are multiples of 6±2 m, suggesting that similar earthquakes of M∼7.5 repeatedly broke this section of the Altyn Tagh Fault. Three such events may have occurred during the 7-17 kyr fast slip period highlighted in Figure 10a, following a 20 kyr-period of lower activity. Earthquake clustering and apparent changes is surface slip rate have been well documented along the Mojave section of the San Andreas Fault in California (Weldon et al., 2004). The 6000 yr-long record of earthquake recurrence at Wrightwood, California showed that the San Andreas fault surface slip rate increased by up to three times the mean slip-rate on the fault during periods of higher seismic activity. There is no such long record of earthquakes along the western section of the Altyn Tagh Fault but such a behavior may explain the apparent slip-rate variations shown in Figure 10a.

Alternatively the variable rate of degradation with distance along the fault could be explained by variations of the diffusion rate through time, forced by changes in climatic conditions during the last glacial and post-glacial periods. This could be the result of an enhancement of the diffusion creep process or the action of other processes such as rain splash or surface runoff. Assuming diffusion is the dominant process at work on the alluvial slopes in the valley, a constant fault slip rate of 2.6 mm/yr would imply that the process was significantly enhanced during the 7.7-11.4 ka period with a mass diffusivity exceeding 10 m^2/ka. Before and after this period, the value of the mass diffusivity was low, consistent with values reported for arid environments Figure 10b. For comparison, Small et al. (1999) report landscape diffusion coefficients as large as 18±2 ka/m^2 for frost-dominated, un-vegetated hillslopes in the Wind River Range, Wyoming.

The origin of the distance axis along the fault was fixed at the intersection point between the fault trace and the T2-T3 riser, a location that is not precisely defined due to the rounded shape of both scarps, thus allowing a possible shift of the time axis in Figure 10b. However, it is remarkable to note that the inferred period of enhanced diffusion on the scarp slope coincides with the warm period identified by the δ^{18}O variations observed in the ice core of the near-by Guliya Ice Sheet (Thompson et al., 1997). In addition, various observations of paleo-shorelines and sediments in Tibetan lakes point to an intensification of the monsoon and warmer and more humid climatic conditions in Central Asia in the early part of the Holocene (Fang, 1991; Gasse et al., 1991). This climatic episode led to the emplacement of the early Holocene fluvial terrace widely observed in the Karakax Valley, but may have also increased the erosion rate of scarps, terrace risers, and other morphological features in the valley.

6 Conclusion

Cosmogenic nuclide and OSL dating methods and analysis of high resolution topography data show that the upper alluvial surface of the Karakax valley is of Eemian age (115±7 kyr) and has been displaced by 300±20 meters by the Altyn Tagh Fault since deposition. This leads to an average slip-rate of 2.6±0.3 mm/yr during that time. This rate is consistent with the mean Holocene rate at a Site 1, west of Shanxili, which may be explained by a constant slip rate on this section of the fault over the last 115 ka. However, the degradation analysis of a fault scarp progressively exposed by slip movement reveals a non-linear relationship between degradation coefficient and distance along the fault strike. We propose two non-exclusive explanations for this observation: First, assuming the mass diffusivity of the landforms to be constant during the last glacial and post glacial periods, a variable surface slip-rate on the fault may account for the observations. Such a rate change can be attributed to seismic clustering, as it has been documented for the Mojave section of the San Andreas Fault in California (Weldon et al., 2004) and suggested to explain the displacement of Holocene landforms along the central Altyn Tagh Fault (Gold et al., 2017). Second, if the slip rate on the fault remained constant, the observations require a variable diffusion rate through time, with an increase of the mass diffusivity constant to a value exceeding 10 ka/m^2 in the early Holocene. Such a high diffusion rate may have been caused by the change of the climatic conditions to a hotter and more humid environment at the end of the last glaciation, as revealed by variations in the δ^{18}O record from the Guliya Ice Cap in the Western Kunlun range (Thompson et al., 1997). The data do not rule out a case where both the fault slip-rate and erosion rate would vary at the same time, with a trade-off between the two effects.

The long-term rate of 2.6±0.3 mm/yr is only 25% of the present-day slip rate of 10.5±1 mm/yr on the western part of the central section of the Altyn Tagh fault (Daout et al., 2018). If the movement of the central section of the fault is transferred to the west into the Karakax section of the fault and the Gozha Co-Longmu Co fault, approximately 75% of the central Altyn Tagh Fault slip rate is required on the latter, exceeding the value of less than 3 mm/yr estimated earlier for this fault (Q. Liu, 1993; Chevalier et al., 2017). Further work will be needed to assess slip-rate stability of western Tibet faults over the Late Quaternary period to reconcile these observations.

Acknowledgments

The field work was carried out in collaboration with Guo Huadong, Wang Chao and Wang Changling from Institut for Remote Sensing and Applications, Diane Evans and Tom Farr from JPL, Oliver Chadwick from UCSB, and Doug Clark from University of Washington. The initial effort was supported by a NASA SIR-C investigation. The OSL sample analysis was supported by the UCLA EPSS department internal funding of the OSL lab. The cosmogenic dating was supported by the Laboratory Directed Research Project (01-ERI-009) at Lawrence Livermore National Laboratory operating under the auspices of the U.S. Department of Energy by Lawrence Livermore National Laboratory under Contract DE-AC52-07NA27344. J.v.d.W. was supported by French Agence Nationale de la Recherche project ANR-10-EQPX-20. The research was in part carried out at the Jet Propulsion Laboratory, California Institute of Technology, under a contract with the National Aeronautics and Space Administration (80NM0018D0004). TanDEM-X topography data were provided by the German Aerospace Center (DLR) via the DLR science portal (https://tandemx-science.dlr.de). Pleiades images (©CNES, 2018, distribution Airbus DS) were obtained via the ESA Earth Online data portal (https://earth.esa.int). Geochronology and topography data resulting from the present study are available on the UCLA Dataverse repository at https://dataverse.ucla.edu/dataverse/atf_kx_landforms_crn_osl. The manuscript benefited from the constructive reviews of Austin Elliott and Marie-Luce Chevalier.

References

Aitken, M. (1985). *Thermoluminescence dating*. London: Academic Press.

Aitken, M. (1998). *Introduction to Optical Dating*. Oxford: Oxford University Press.

Andrews, D. J., & Hanks, T. C. (1985). Scarp degraded by linear diffusion: Inverse solution for age. *Journal of Geophysical Research: Solid Earth*, *90*(B12), 10193-10208. doi: 10.1029/JB090iB12p10193

Armijo, R., Tapponnier, P., & Han, T. (1989). Late cenozoic right-lateral strike-slip faulting in southern tibet. *Journal of Geophysical Research: Solid Earth*, *94*(B3), 2787-2838. doi: 10.1029/JB094iB03p02787

Avouac, J. P. (1993). Analysis of scarp profiles: Evaluation of errors in morphologic dating. *Journal of Geophysical Research: Solid Earth*, *98*(B4), 2787-2838. doi: 10.1029/92JB01962

Balco, G., Stone, J. O., Lifton, N. A., & Dunai, T. J. (2008). A complete and easily accessible means of calculating surface exposure ages or erosion rates from ^{10}Be and ^{26}Al measurements. *Quaternary Geochronology*, *3*, 174-195.

Bell, W. T. (1979). Attenuation factors for the absorbed radiation dose in quartz inclusions for thermoluminescence dating. *Ancient TL*, *8*, 1–12.

Bevington, P. R., & Robinson, D. K. (2002). *Data reduction and error analysis for physical sciences*. New York: McGraw-Hill. doi: 10.1119/1.17439

Beyer, R. A., Alexandrov, O., & McMichael, S. (2018). The Ames Stereo Pipeline: NASA's open source software for deriving and processing terrain data. *Earth and Space Science*, *5*, 537-548. doi: 10.1029/2018EA000409

Borchers, B., Marrero, S., Balco, G., Caffee, M., Goehring, B., Lifton, N., ... Stone, J. (2016). Geological calibration of spallation production rates in the CRONUS-Earth project. *Quaternary Geochronology*, *31*, 188-198. doi: 10.1016/j.quageo.2015.01.009

Brennan, B. J., Lyons, R. G., & Phillips, S. W. (1991). Attenuation of alpha particle track dose for spherical grains. *Nuclear Tracks and Radiation Measurements*, *18*, 249–253.

Bull, W. B. (1999). *Geomorphic response to climate change*. New York: Oxford University Press.

Bull, W. B. (2007). *Tectonic geomorphology of mountains: A new approach to paleoseismology*. Hoboken, NJ: Wiley-Blackwell. doi: 10.1002/9780470692318

Burow, C. (2019). calcMaxDose(): Apply the maximum age model to a given De distribution. Function version 0.3.1. In: Kreutzer, S., Burow, C., Dietze, M., Fuchs, M.C., Schmidt, C., Fischer, M., Friedrich, J., 2019. Luminescence: Comprehensive Luminescence Dating Analysis. R package version 0.9.3.

Buylaert, J., Murray, A., Thomsen, K., & Jain, M. (2009). Testing the potential of an elevated temperature IRSL signal from K-feldspar. *Radiat. Meas.*, *44*(5-6), 560–565. Retrieved from `http://www.sciencedirect.com/science/article/pii/S1350448709000316` doi: 10.1016/j.radmeas.2009.02.007

Centre National d'Etudes Spatiales. (2016). *Pleiades: Two satellites to observe Earth close up.* Retrieved 2019-08-24, from `https://Pleiades.cnes.fr/en/PLEIADES/index.htm`

Chevalier, M. L., Pan, J. W., Li, H. B., Sun, Z., Liu, D. L., Pei, J. L., ... Wu, C. (2017). First tectonic-geomorphology study along the Longmu-Gozha Co fault system, Western Tibet. *Gondwana Research*, *41*, 411-424. doi: 10.1016/j.gr.2015.03.008

Chmeleff, J., von Blanckenburg, F., Kossert, K., & Jakob, D. (2010). Determination of the 10Be half-life by multicollector ICP-MS and liquid scintillation counting. *Nuclear Instruments and Methods in Physics Research Section B: Beam Interactions with Materials and Atoms*, *268*, 192-199. doi: 10.1016/j.nimb.2009.09.012

Cowgill, E. (2007). Impact of riser reconstruction on estimation of secular variation in rates of strike-slip faulting: Revisiting the Cherchen river site along the

Altyn Tagh fault, NW China. *Earth Planet. Sci. Lett.*, *254*, 239-255.
Dahl-Jensen, D., Albert, M. R., Aldahan, A., Azuma, N., Balslev-Clausen, D., Baumgartner, M., ... Zheng, J. (2013). Emian interglacial reconstructed from a Greenland folded ice core. *Nature.*, *493*, 489-494. doi: 10.1038/nature11789
Daout, S., Doin, M.-P., Peltzer, G., Lasserre, C., Socquet, A., Volat, M., & Sudhaus, H. (2018). Strain partitioning and present-day fault kinematics in nw tibet from envisat sar interferometry. *J. Geophys. Res.*, *123*(3), 2462-2483. doi: 10.1002/2017JB015020
Duller, G. A. T. (2004). Luminescence dating of quaternary sediments: recent advances. *Journal of Quaternary Science*, *19*(2), 183-192. Retrieved from `https://onlinelibrary.wiley.com/doi/abs/10.1002/jqs.809` doi: 10.1002/jqs.809
Durcan, J. A., King, G. E., & Duller, G. A. T. (2015). DRAC: Dose Rate and Age Calculator for trapped charge dating. *Quat. Geochronol.*, *28*, 54–61.
Fang, J.-Q. (1991). Lake evolution during the past 30,000 years in China, and its implications for environmental change. *Quaternary Research*, *36*, 37-60.
Farr, T., & Chadwick, O. (1996). Geomorphic processes and remote sensing signatures of alluvial fans in the Kunlun Mountains, China. *J. Geophys. Res.*, *101*(E10), 23,091-23,100.
Galbraith, R. F., Roberts, R. G., Laslett, G. M., Yoshida, H., & Olley, J. M. (1999). Optical dating of single and multiple grains of quartz from Jinmium rock shelter, northern Australia: Part i, experimental design and statistical models. *Archaeometry*, *41*(2), 339–364. doi: 10.1111/j.1475-4754.1999.tb00987.x
Gasse, F., Arnold, M., Fontes, J., Fort, M., Gibert, E., Huc, A., ... Zhang, Q. (1991). A 13,000-year climate record from western Tibet. *Nature.*, *353*, 742-745.
Gold, R., Cowgill, E., Arrowsmith, R., & Friedrich, A. (2017, 2 1). Pulsed strain release on the altyn tagh fault, northwest china. *Earth and Planetary Sciences Letters*, *459*, 291–300. doi: 10.1016/j.epsl.2016.11.024
Gong, Z., Sun, J., Zhang, Z., Fu, B., & Jia, Y. (2017). Optical dating of an offset river terrace sequence across the karakax fault and its implication for the late quaternary left-lateral slip rate. *Journal of Asian Earth Sciences*, *147*, 415-423. doi: 10.1016/j.jseaes.2017.07.013
Guérin, G., Mercier, N., Nathan, R., Adamiec, G., & Lefrais, Y. (2012). On the use of the infinite matrix assumption and associated concepts: A critical review. *Radiat. Meas.*, *47*, 778–785. doi: 10.1016/j.radmeas.2012.04.004
Guilbaud, C., Simoes, M., Barrier, L., Laborde, A., Van der Woerd, J., Li, H., ... Murray, A. (2017). Kinematics of active deformation across the western kunlun mountain range (xinjiang, china) and potential seismic hazards within the southern tarim basin. *Journal of Geophysical Research: Solid Earth*, *122*(12), 10,398-10,426. Retrieved from `https://agupubs.onlinelibrary.wiley.com/doi/abs/10.1002/2017JB014069` doi: 10.1002/2017JB014069
Hajnsek, I., Busche, T. E., Krieger, G., Zink, M., & Moreira, A. (2014). *TanDEM-X Ground Segment Announcement of Opportunity: TanDEM-X Science Phase.* Retrieved 2016-08-24, from `https://tandemx-science.dlr.de/pdfs/TD-PD-PL_0032TanDEM-X_Science_Phase.pdf`
Hilley, G. E., DeLong, S., Prentice, C., Blisniuk, K., & Arrowsmith, J. (2010). Morphologic dating of fault scarps using airborne laser swath mapping (ALSM) data. *Geophys. Res. Lett.*, *37*(L04301), 1-6. doi: 10.1029/2009GL042044
Huntley, D. J., & Baril, M. R. (1997). The K content of the K-feldspars being measured in optical dating or in thermoluminescence dating. *Ancient TL*, *15*(1), 11–13.
Imbrie, J., Hays, J. D., Martinson, D. G., McIntyre, A., Mix, A. C., Morley, J. J., ... Shackleton, N. J. (1984). *The orbital theory of pleistocene climate: support from a revised chronology of the marine d18o record.* Dordrecht: D. Reidel

Publishing Company.
Kohl, C. P., & Nishiizumi, K. (1992). Chemical isolation of quartz for measurement of in situ-produced cosmogenic nuclides. *Geochimica Et Cosmochimica Acta*, *56(9)*, 3583-3587.
Korschinek, G., Bergmaier, A., Faestermann, T., Gerstmann, U. C., Knie, K., Rugel, G., … von Gostomski, C. L. (2010). A new value for the half-life of ^{10}Be by heavy-ion elastic recoil detection and liquid scintillation counting. *Nuclear Instruments and Methods in Physics Research Section B: Beam Interactions with Materials and Atoms*, *268(2)*, 187-191. doi: 10.1016/j.nimb.2009.09.020
Lal, D. (1991). Cosmic-ray labeling of erosion surfaces - in situ nuclide production-rates and erosion models. *Earth Planet. Sci. Lett.*, *104(2-4)*, 424-439.
Lasserre, C., Morel, P. H., Gaudemer, Y., Tapponnier, P., Ryerson, F. J., King, G. C. P., … Yuan, D. (1999). Postglacial left slip-rate and past occurrence of M≥8 earthquakes on the western Haiyuan fault, Gansu, China. *J. Geophys. Res.*, *104*, 17,633-17,651. doi: 10.1029/1998JB900082
Li, H., Van der Woerd, J., Sun, Z., Mériaux, A. S., Tapponnier, P., Ryerson, F., … Pan, J. (2008). The Kangxiwa section of the Altun Fault zone since the Quaternary, left slip rate and the recurrence period of large earthquakes. *Quaternary Sciences*, *28*(2), 197-213.
Li, H., Van der Woerd, J., Sun, Z., Si, J., Tapponnier, P., Pan, J., … Chevalier, M.-L. (2012). Co-seismic and cumulative offsets of the recent earthquakes along the Karakax left-lateral strike-slip fault in western Tibet. *Gondwana Research*, *21*, 64-87. doi: 10.1016/j.gr.2011.07.025
Lifton, N., Sato, T., & Dunai, T. J. (2014). Scaling in situ cosmogenic nuclide production rates using analytical approximations to atmospheric cosmic-ray fluxes. *Earth Planet. Sci. Lett.*, *386*, 149-160.
Liritzis, I., Stamoulis, K., Papachristodoulou, C., & Ioannides, K. (2013). A re-evaluation of radiation dose-rate conversion factors. *Mediterranean Archaeology and Archaeometry*, *13*, 1–15.
Liu, J. (2011). Kunlun mountains. In V. Singh, P. Singh, & U. Haritashya (Eds.), *Encyclopedia of snow, ice and glaciers. encyclopedia of Earth sciences series* (p. 679-682). Springer, Dordrecht. doi: 10.1007/978-90-481-2642-2
Liu, Q. (1993). *Palé oclimat et contraintes chronologiques sur les mouvements récents dans l'Ouest du Tibet: failles du Karakorum et de Longmu Co-Gozha Co, lacs en pull-apart de Longmu Co et de Sumxi Co.* (Dissertation). University of Paris VII.
Mériaux, A. S., Tapponnier, P., Ryerson, F. J., Xu, X., King, G., Van der Woerd, J., … Chen, W. (2005). The Aksay segment of the northern Altyn Tagh fault: Tectonic geomorphology, landscape evolution, and holocene slip rate. *J. Geophys. Res.*, *110*(B04404), 1-32. doi: 10.1029/2004JB003210
Mériaux, A. S., Van der Woerd, J., Tapponnier, P., Ryerson, F. J., Finkel, R. C., Lasserre, C., & Xu, X. (2012). The Pingding segment of the Altyn Tagh Fault (91°E): Holocene slip-rate determination from cosmogenic radionuclide dating of offset fluvial terraces. *J. Geophys. Res.*, *117*(B09406), 1-26. doi: 10.1029/2012JB009289
Molnar, P., & Tapponnier, P. (1975). Cenozoic tectonics of asia: Effects of a continental collision. *Science.*, *189*(4201), 419–426. doi: 10.1126/science.189.4201.419
Nakawo, M., Ageta, Y., & Han, J. K. (1990). Climatic information from Chongce ice cap, the West Kunlun, China. *Annals of Glaciology*, *14*, 205-207.
Nash, D. B. (1980). Morphologic dating of degraded normal fault scarps. *The Journal of Geology*, *88*(3), 353-360. doi: 10.1086/628513
Nishiizumi, K., Winterer, E. L., Kohl, C. P., Lal, D., Arnold, J. R., Klein, J., & Middelton, R. (1989). Cosmic ray production rates of ^{10}Be and ^{26}Al in quartz from glacially polished rocks. *J. Geophys. Res.*, *94*, 17,907-17,915.

Peltzer, G., Tapponnier, P., & Armijo, R. (1989, DEC 8). Magnitude of late quaternary left-lateral displacement along the north edge of Tibet. *Science.*, *246*(4935), 1285-1289. doi: {10.1126/science.246.4935.1285}

Phillips, F. M., Hinz, M., Marrero, S. M., & Nishiizumi, K. (2016). Constraints on cosmogenic nuclide production rates by samples from the sierra nevada, california: Ii. sample sites and evaluation. *Quaternary Geochronology*, *32*, 101-118.

Porat, N., Faerstein, G., Medialdea, A., & Murray, A. S. (2015). Re-examination of common extraction and purification methods of quartz and feldspar for luminescence dating. *Ancient TL*, *33*, 22–30.

Ryerson, F. J., Peltzer, G., Tapponnier, P., Finkel, R., Mériaux, A., & Van der Woerd, J. (1999). Active slip-rates on the Altyn Tagh fault - Karakax valley segment: Constraints from surface exposure dating [Abstract]. *Eos Trans. AGU.*.

Ryerson, F. J., Tapponnier, P., Finkel, R. C., Mériaux, A.-S., Van der Woerd, J., Lasserre, C., ... King, G. C. (2006, 01). Applications of morphochronology to the active tectonics of Tibet. In *In Situ-Produced Cosmogenic Nuclides and Quantification of Geological Processes.* Geological Society of America. Retrieved from `https://doi.org/10.1130/2006.2415(05)` doi: 10.1130/2006.2415(05)

Small, E., Anderson, R., & Hancock, G. (1999). Estimates of the rate of regolith production using 10Be and 26Al from an alpine hillslope. *Geomorphology*, *27*, 131-150.

Stone, J. O. (2000). Air pressure and cosmogenic isotope production. *J. Geophys. Res.*, *105(B10)*, 23,753-23,759. doi: 10.1029/2000JB900181

Tapponnier, P., & Molnar, P. (1977). Active faulting and tectonics in China [Article]. *J. Geophys. Res.*, *82*(20), 2905-2930. doi: {10.1029/JB082i020p02905}

Tapponnier, P., Xu, Z., Roger, F., Meyer, B., Arnaud, N., Wittlinger, G., & Yang, J. (2001, 11). Oblique stepwise rise and growth of the tibet plateau. *Science*, *294*, 1671-1677. doi: 10.1126/science.105978

Thompson, G., Yao, T., Davis, M., Henderson, K., Mosley-Thompson, E., Lin, P.-N., ... Bolzan, J. (1997). Tropical climate instability: The last glacial cycle from a Qinghai-Tibetan ice core. *Science.*, *276*, 1821-1825. doi: 10.1126/science.276.5320.1821

Van Der Woerd, J., Ryerson, F. J., Tapponnier, P., Gaudemer, Y., Finkel, R., Mériaux, A. S., ... He, Q. (1998). Holocene left slip-rate determined by cosmogenic surface dating on the Xidatan segment of the Kunlun Fault (Qinghai, China). *Geology*, *26*, 695-698.

Van Der Woerd, J., Tapponnier, P., Ryerson, F. J., Mériaux, A.-S., Meyer, B., Gaudemer, Y., ... Zhiqin, X. (2002). Uniform postglacial slip-rate along the central 600km of the Kunlun fault (Tibet), from 26 Al, 10 Be, and 14 C dating of riser offsets, and climatic origin of the regional morphology. *Geophys. J. Int.*, *148*, 356-388.

Wallace, R. (1977). Profiles and ages of young fault scarps, north-central Nevada [Article]. *Geol. Soc. Am. Bull.*, *88*, 1267-1281.

Weldon, R., Scharer, K., Fumal, T., & Biasi, G. (2004). Wrightwood and the earthquake cycle: What a long recurrence record tells us about how faults work [Article]. *GSA Today*, *14*(9), 4-10. doi: 10.1130/1052-5173(2004)014

Winograd, I. J., Landwehr, J. M., Ludwig, K. R., Coplen, T. B., & Riggs, A. C. (1997). Duration and structure of the past four interglaciations. *Quaternary Research*, *48*(2), 141–154. doi: 10.1006/qres.1997.1918

Wintle, A. G. (1997). Luminescence dating: laboratory procedures and protocols. *Radiation Measurements*, *27*(5), 769 - 817. Retrieved from `http://www.sciencedirect.com/science/article/pii/S1350448797002205` doi: https://doi.org/10.1016/S1350-4487(97)00220-5